

UNIVERSIDADE ESTADUAL DE CAMPINAS
SISTEMA DE BIBLIOTECAS DA UNICAMP
REPOSITÓRIO DA PRODUÇÃO CIENTÍFICA E INTELECTUAL DA UNICAMP

Versão do arquivo anexado / Version of attached file:

Versão do Editor / Published Version

Mais informações no site da editora / Further information on publisher's website:

<https://link.springer.com/article/10.1007/s40962-023-01145-z>

DOI: <https://doi.org/10.1007/s40962-023-01145-z>

Direitos autorais / Publisher's copyright statement:

©2023 by American Foundry Society. All rights reserved.

DIRETORIA DE TRATAMENTO DA INFORMAÇÃO


Cidade Universitária Zeferino Vaz Barão Geraldo

CEP 13083-970 – Campinas SP

Fone: (19) 3521-6493

<http://www.repositorio.unicamp.br>

THE EFFECTS OF COOLING RATE ON MICROSTRUCTURE FORMATION DURING SOLIDIFICATION OF 319 ALLOY

Izabel da Penha Gomes, André Barros , Gabriela Lujan Brollo , Cássio Augusto Pinto da Silva , Noé Cheung  and Eugênio José Zoqui 

Materials and Manufacturing Department, Faculty of Mechanical Engineering, University of Campinas – UNICAMP, Campinas, SP 13083-860, Brazil

Copyright © 2023 The Author(s)
<https://doi.org/10.1007/s40962-023-01145-z>

Abstract

This work assesses the effect of cooling rate (\dot{T}) on the solidification kinetics and microstructural evolution of a 319 aluminum alloy with and without the addition of Al–5 wt%Ti–1wt%B grain refiner. Directionally solidified samples were produced under various cooling rates (from 0.05 to 40 °C/s). Microstructure coarsening was then quantitatively analyzed by measuring grain size (GS) and primary (λ_1), secondary (λ_2) and average (λ_L) dendrite arm spacing. The results show that polarized optical images can be used to identify dendrite fragments between neighboring primary dendrites, allowing a more accurate microstructural analysis after the addition of grain refiner.

The results also show that, for a given \dot{T} , although GS is reduced after the addition of grain refiner, the respective values of λ_1 , λ_2 and λ_L remain practically the same. In other words, the grain refiner only affects nucleation and not grain growth. Experimental growth equations are proposed to represent this behavior. Furthermore, λ_L is shown to be a good parameter for evaluating microstructural refinement.

Keywords: microstructure, 319 alloy, solidification, dendritic growth, grain refining

Introduction

Because of their exceptional combinations of properties, such as high strength-to-weight ratio associated with outstanding castability, excellent wear performance and high recyclability, Al-based alloys find widespread use in both the aerospace and automotive industries.¹ Among these alloys, 319 Al alloy (Al–Si–Cu based) deserves special attention. The composition of this alloy is of particular interest in the manufacture of engine blocks because of its low density, good mechanical strength at relatively high temperatures and suitable wear resistance.^{2,3} Without reliable control of the microstructure, however, the optimized properties of products made from 319 alloy cannot be totally guaranteed.⁴

In processes such as conventional sand casting, die casting, welding and additive manufacturing, Al–Si–Cu alloys used to manufacture components with different shapes and sizes

usually undergo solidification. Control of the cooling rate (\dot{T}) during these processes is of practical importance since the rate at which the temperature decreases plays a key role in the evolution of the microstructure. This is also true for rheocasting (directly) and for thixoforming (prior to forming, during the feedstock preparation step) as \dot{T} directly affects the microstructure of the semisolid slurry, which should consist of as fine and globular a solid phase as possible within the liquid for adequate thixotropy.^{5–7}

One of the most important microstructural features observed in many castings is the dendritic microstructure. Over the past years, significant efforts have been made to achieve a better understanding of dendrite growth during directional solidification of several Al-based alloys.^{8–13} The key parameters used in dendrite growth analysis are primary (λ_1), secondary (λ_2) and tertiary (λ_3) dendrite spacing, which are related to thermal solidification parameters such as \dot{T} .^{9–18} Dendrite spacing is widely known to be a determining factor for many mechanical properties.^{8,13} For example, λ_2 is known to affect the permeability of semisolid structures.¹⁶ However, very few of

these studies focused on the effect of the addition of grain refiners.

The use of grain refiners of different types, such as Al–Ti–B or Al–Ti–C, with Al-based alloys is a fundamental practice in the foundry industry and should therefore be the subject of study.^{9–24} An excellent strategy for systematic investigation into the effects of these grain refiners is the use of transient directional solidification techniques as with only one experimental run a wide range of \dot{T} can be achieved along the length of the casting and, in turn, a wide range of a microstructural scales. This experimental approach is adopted here to compare the evolution of the solidification microstructure of 319 alloy with and without Al–5 wt% Ti–1 wt% B grain refiner, referred to here as 319R and 319, respectively. One of the main contributions of this work is the application of the dendrite growth theory to predict and control casting, die casting, rheocasting and feedstock preparation parameters for thixoforming operations.

Experimental Procedure

The chemical composition of the 319 alloy studied here was determined with a BILL OES optical spectrophotometer and is shown in Table 1. First, 750 g of the 319 alloy was put in a SiC crucible, which was then placed in a muffle furnace set to 750 °C. For the experiments with grain refiner, when the alloy had melted completely, the crucible was taken out of the furnace and a stoichiometric amount of an Al–5wt%Ti–1wt%B master alloy was added to the liquid to achieve a Ti solute content of 0.2 wt%. Next, the molten alloy was mechanically homogenized with a stainless-steel bar coated with alumina and poured into a mold inside a directional solidification apparatus^{15–17}. Figure 1a presents a schematic overview of the solidification device. After the pouring procedure, argon was injected into the melt for at least 3 minutes to remove trapped gases.

Unsteady-state solidification experiments with the 319 and 319R alloy were carried out in the directional solidification apparatus, in which an electrical resistance around the mold allows the temperature of the melt to be controlled and ensures that heat is only extracted through a water-cooled bottom made of AISI 1020 steel following the same procedures described in previous articles.^{15–17,26,27} Prior to mold assembly, the inner surface of the mold's bottom part (which was intended to come into contact with the molten alloy) was metallographically ground to achieve a standardized finishing using 1200-grit SiC abrasive paper. A stainless-steel mold with an internal diameter of 55 mm, a height of 110 mm and a wall thickness of 5 mm was used. The mold was constructed using two AISI 310 stainless-steel half-cylindrical shells, which were joined together using M6 screws and nuts. Along the height of the mold, eight through holes were designed for positioning type K thermocouples with an outer diameter of 1.6 mm. These thermocouples allowed for the temperature monitoring during solidification. Figure 1b provides a schematic illustration showcasing the precise dimensions of the mold, the locations of the thermocouples and details of the water-cooled bottom part. To avoid radial temperature gradients and facilitate casting removal, a ceramic coating was applied to the inner vertical surface of the mold. When the melt temperature was 10% higher than the liquidus temperature, the electric heaters were disconnected and the water-flow system turned on so that solidification could start.

Real-time temperature during solidification was monitored with a set of fine K-type thermocouples (1.6 mm external diameter) placed along the length of the castings at 15mm deep and connected by coaxial cables to a Lynx ADS1000 data logger. Temperature-time data were recorded at a frequency of 5 Hz and used with well-known techniques²⁸ to determine the cooling rate (\dot{T}) when the liquidus isotherm passed each thermocouple. Basically, \dot{T} values were calculated using the derivative with respect to time of fitted

Table 1. Chemical Composition of the 319 Alloy Studied

Alloy		Element (wt%)									
		Si	Cu	Fe	Mg	Zn	Mn	Ni	Ti	Res ^a	Al ^b
319 ^d	Min.	5.50	3.00	0	0	0	0	0	0	0	81.5
	Exp. ^c	5.92	3.54	0.43	0.15	0.36	0.34	0.25	0.05	0.18	88.8
		± 0.12	± 0.10	± 0.03	± 0.01	± 0.01	± 0.01	± 0.01	± 0.01		
	Max.	6.50	4.00	0.80	0.10	1.0	0.5	0.35	0.25	0.5	86.25

Standard uncertainties are shown as the deviation corresponding to a 0.95 confidence interval. The max. and min. limits shown are those specified in ²⁵.

^aSum of residual elements

^bBalance

^cExperimental

^dAccording to ASTM B179-18, the alloy is 319.1.

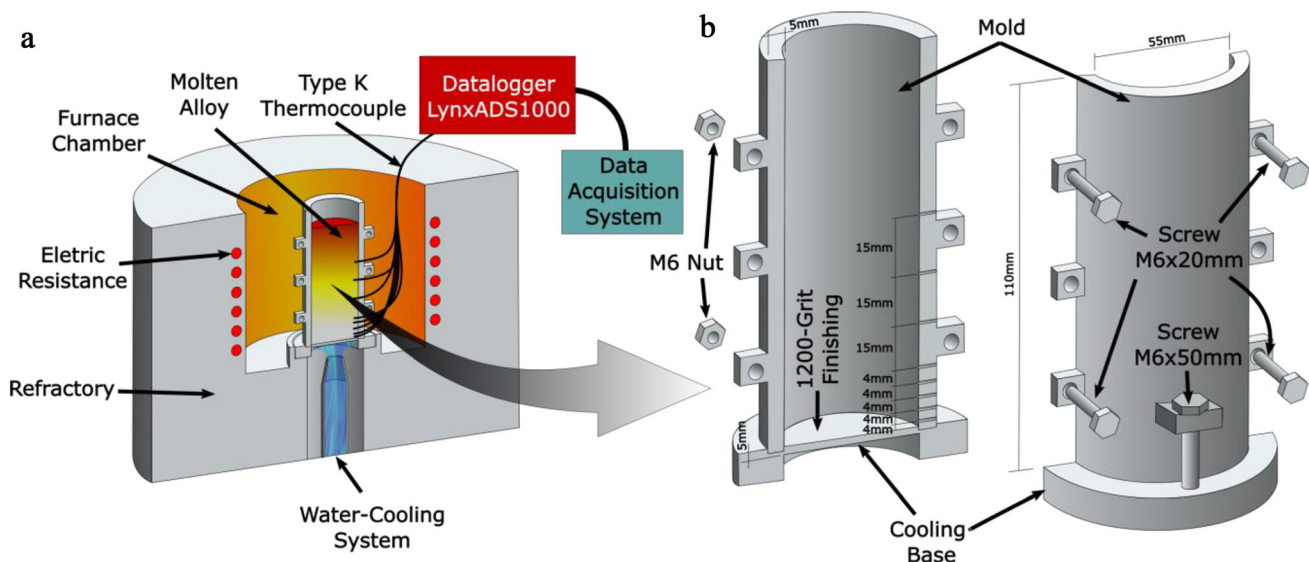


Figure 1. Scheme of the (a) directional solidification device and (b) mold used in this study.

regression profiles that represented the trend lines of the cooling curves in a comprehensive region around the liquidus temperature ($\pm 15\text{ }^{\circ}\text{C}$) with a coefficient of determination (R^2) greater than 0.9.

For macrographic examination, the directionally solidified (DS) 319 alloy casting was sectioned along its vertical axis, and one of the semicylindrical parts was ground with 100- to 1200-grit soft SiC papers and then etched with aqua regia solution (3:1 mixture of HCl and HNO₃, respectively). For microstructural characterization, selected cross sections at different positions in relation to the metal/mold interface were extracted from the DS casting. The microstructure of the alloy was evaluated after polishing down to $0.1\text{ }\mu\text{m}$ with a metallographic vibratory polisher. Conventional metallography in black and white (B&W) involved solely polishing, while for color metallography the samples were subjected to electrolytic etching with a 1.8% HBF₄ solution under mechanical stirring at 0.6 A and 30 V for 180 s. Polarizing filters were used to obtain color images allowing dendrites with varying crystal orientations to exhibit distinct colors. In both cases, a Leica DM ILM microscope was employed for observation.

Dendrite arm spacing was measured in longitudinal and transverse cross sections of samples extracted along the length of the DS castings. The triangle method²⁹ was used with ImageJ to measure primary dendrite arm spacing (λ_1) in transverse cross sections, while the intercept method was used to measure average grain size (GS) and average arm spacing (λ_L) in transverse cross sections, although the secondary arm spacing (λ_2) was measured in the longitudinal sections (approximately 50 and 200 measurements were taken for each selected longitudinal and transverse position, respectively).³⁰ Note that the average arm spacing (λ_L) is measured using the Heyns intercept method and

represents the average distance between two consecutive branches of the dendritic structure, disregarding if represents the primary or secondary arm spacing.

Results and Discussion

In Figure 2a, the white vertical line indicates the composition of the 319 alloy in the partial phase diagram determined by Thermo-Calc[®] (V 5.01.61) computational thermodynamics software with the TTAL5 database. Starting from the liquid, an Al-rich primary phase (Al_{FCC} for low silicon content and Al_α for high silicon) is formed in the area highlighted in dark green), followed by a Si-rich main eutectic. Further tertiary eutectic phases consisting mainly of AlFeSi-β and small amounts of Al₃Ni₂ are formed at lower temperatures. The simulation also provides the liquidus (610.8 °C) and solidus (502.8 °C) temperatures of the alloy. The elements Al, Si, Cu, Fe, Mg, Zn, Mn, Sn, Ni and Cr were considered in the simulation. At room temperature, Thermo-Calc[®] predicts the existence of Al_α and the Al/Si eutectic phase, as well as the AlFeSi-β and small amounts Al₂Cu, Al₅Cu₂Mg and Al₇Cu₄Ni in addition to TiAl₃, especially for the chemical refined 319R structure. This evaluation aims to provide the reader an idea of the possible metallic phases that can be found in the material under analysis and represents a calculation of the equilibrium phases.

Figure 2b shows the characteristic as-solidified microstructure of the 319 alloy. The microstructure is essentially formed of dendrite-like Al-rich primary phase (A) and intergranular Si-rich main eutectic (B) as predicted by Thermo-Calc[®]. Tertiary eutectic compounds are found in the interdendritic space, including acicular AlFeSi-β phase (C), platelets of θ-Al₂Cu(Si) phase preferentially

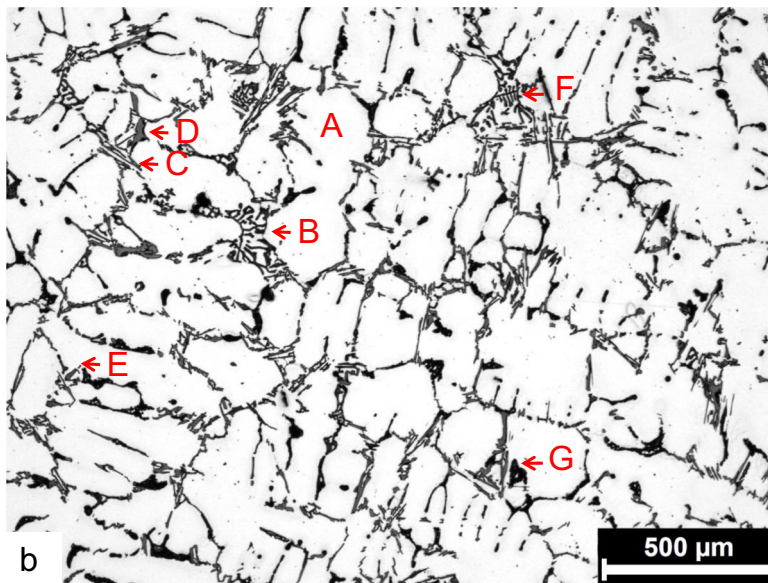
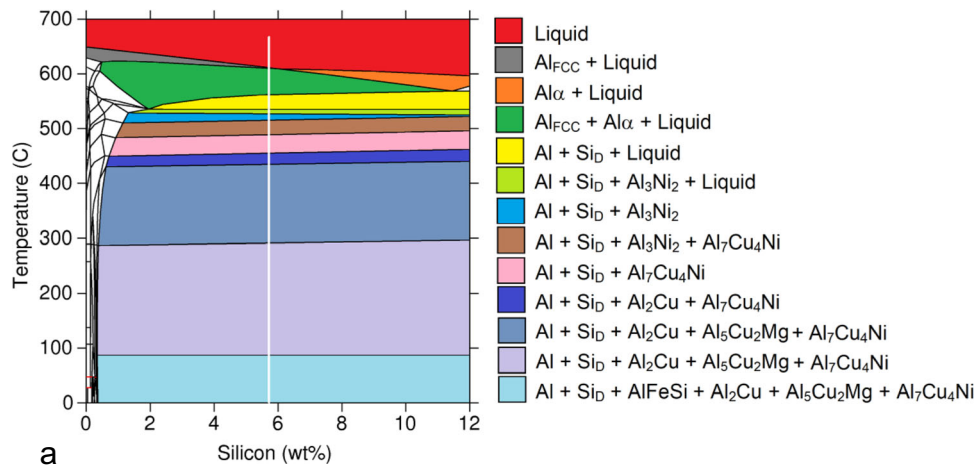


Figure 2. Phase diagram at thermodynamic equilibrium for the 319 alloy (a). Typical microstructure of the 319 alloy (b) in the as-polished condition.

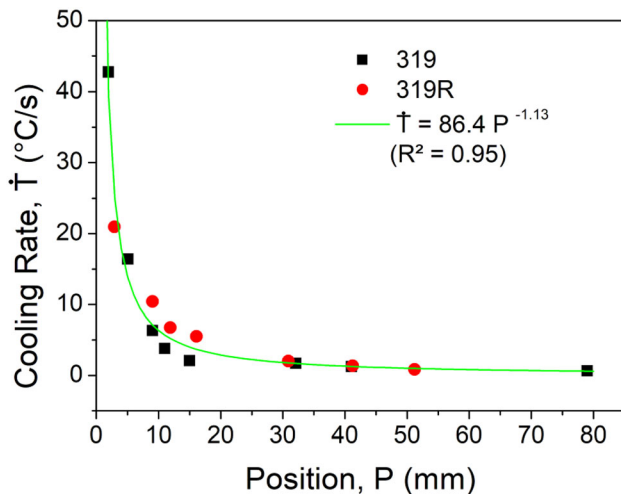


Figure 3. Experimental profile of \dot{T} along the length of the 319 and 319R alloys castings.

nucleated around β -phase (D) and clusters of Cu-rich Al–Al₂Cu–Si phase (E). In addition, the complex Al₁₅(FeMnCr)₃Si₂ compound (known as α -Fe phase) is present in the form of both Chinese (F) script and polyhedral morphologies (G) which differs from the microstructure predicted by Thermo-calc[®]; in fact, kinetic factors can sometimes result in the formation of non-equilibrium phases.^{30,31}

Figure 3 shows the solidification cooling rate (\dot{T}) profile along the length of the DS casting alloys with and without Al–5Ti–1B [wt%] grain refiner (319 and 319R). To determine the points in the graph, the liquidus (610.8 °C) and solidus (502.8 °C) were considered to be the limits of the solidification range. As can be seen, it was possible in only one experimental run to achieve a wide range of \dot{T} from approximately 0.5 to 45 °C/s, values commonly found in the literature on commercial sand casting and die

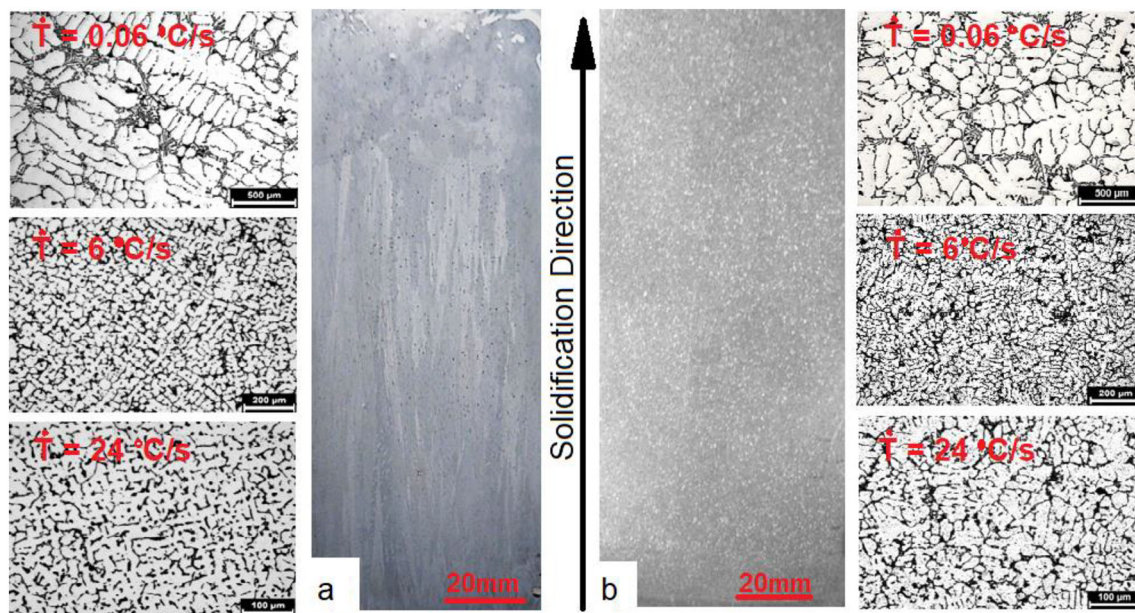


Figure 4. Macrostructure of the (a) 319 and (b) 319R alloy castings along with their characteristic microstructures.

casting.^{1,10,18} Figure 3 also shows that the addition of grain refiner did not have a significant effect on \dot{T} ; in fact, a single experimental power equation is able to represent the dataset for both experiments:

$$\dot{T} = 86.4 P^{-1.13} \quad (^\circ\text{C/s}, R^2 = 0.95), \quad \text{Eqn. 1}$$

where P is the position in mm.

Columnar grains prevailed along the entire length of the DS 319 alloy casting analyzed (Figure 4a). However, after the addition of grain refiner, the macrostructural morphology changed to equiaxed structure with finer grain size (Figure 4b). In the case of the 319R alloy, the absence of aligned grains prevented any analysis of vectorial thermal parameters such as the growth rate (v) and thermal gradient ($G = \dot{T}/v$). For this reason and for practical purposes, \dot{T} is the only thermal parameter considered for analysis here.

Figures 5 and 6 show representative micrographs of the 319 and 319R alloys, respectively. These images, obtained from cross sections of the castings, correspond to several \dot{T} values. As expected, an increase in \dot{T} led to a more refined structure. However, this effect differs considerably between the samples with and without grain refiner. While the magnification used in the color images is the same for all the conditions as this allows the grains to be more easily observed, the magnification in the B&W images was increased as \dot{T} increased so that the microstructure could be more readily observed and the effect of the thermal parameters on dendrite spacing could be compared. Note that the increase in \dot{T} promotes refinement of the dendrite arms (left) and grains (right) that constitute the microstructure of the alloys.

The grain refining effect is clearly more pronounced in the refined alloy (Figure 6) than in the unrefined alloy (Figure 5). In fact, the observed grain size in refined structures is half that found in unrefined structures. This effect is also observed in the B&W images, where the dendrite morphology varies from quite coarse to fine. For the microstructural analysis, micrographs like those shown in Figures 5 and 6 were used to measure the microstructural parameters studied here, namely, primary, secondary and average dendrite arm spacing and grain size (λ_1 , λ_2 , λ_L , GS). Unlike the other measurements, which were taken in transverse cross sections, the secondary dendrite spacing of the 319 and 319R alloys was measured using images obtained from longitudinal cross sections of the ingots, as shown later in this work.

In the color micrographs, where the grains can be observed in both the alloys, the microstructure starts out extremely coarse and decreases in size as one moves toward regions subjected to higher \dot{T} . Although this is true for both alloys, in the case of the 319R alloy the effect of the grain refiner can already be observed even for low cooling rates. For higher rates, such as in die casting operations, the refined microstructure of 319R has the lowest observed GS, with grains in the 100 μm range.

Figure 7 shows the relationship between grain size and cooling rate (average \pm standard deviation, trend line and experimental equation) of the microstructural parameters (GS, λ_1 , λ_L and λ_2) in relation to \dot{T} during solidification of the 319 and 319R alloys. Addition of grain refiner clearly has a significant impact on GS. For a given value of \dot{T} , the GS of the 319R alloy is about 54% smaller than that of the

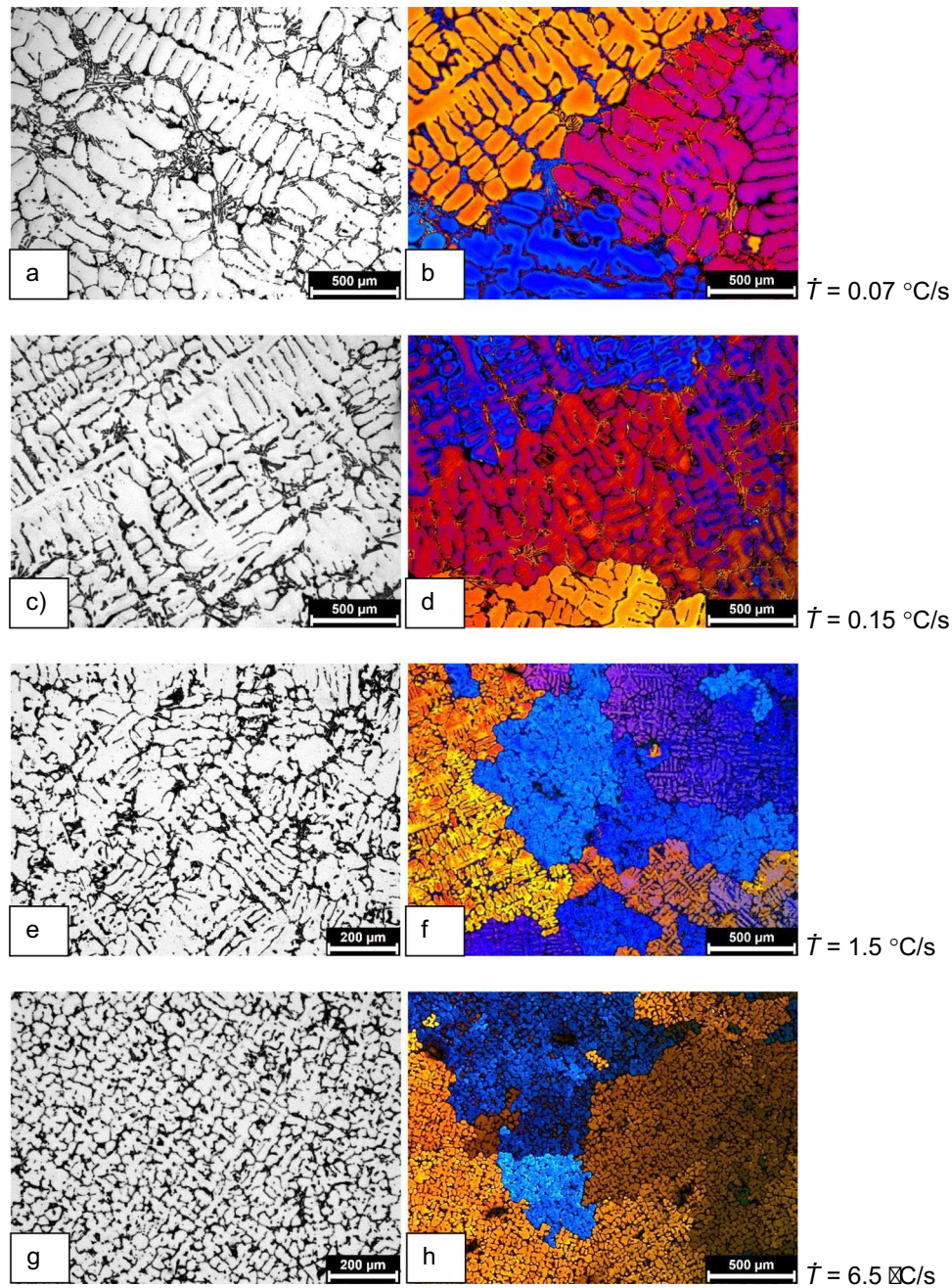


Figure 5. Microstructural evolution of 319 alloy with increasing cooling rate. Conventional B&W micrographs and color micrographs taken under polarized light for cooling rates of: (a) and (b) $\dot{T} = 0.07 \text{ }^{\circ}\text{C/s}$; (c) and (d) $\dot{T} = 0.15 \text{ }^{\circ}\text{C/s}$; (e) and (f) $\dot{T} = 1.5 \text{ }^{\circ}\text{C/s}$; (g) and (h) $\dot{T} = 6.5 \text{ }^{\circ}\text{C/s}$; (i) and (j) $\dot{T} = 13 \text{ }^{\circ}\text{C/s}$; (k) and (l) $\dot{T} = 23 \text{ }^{\circ}\text{C/s}$; (m) and (n) $\dot{T} = 37.5 \text{ }^{\circ}\text{C/s}$; and (o) and (p) $\dot{T} = 84.5 \text{ }^{\circ}\text{C/s}$.

319 alloy. For unrefined samples, there is a very large dispersion of the data, which is reflected in the standard deviation. Grain refining combined with a higher cooling rate resulted in a more homogeneous microstructure.

The addition of grain refiner, however, had little or no effect on λ_1 , λ_L and λ_2 , and the cooling rate was the main

parameter that could be used to control the structure. For GS, we therefore have the following equations (Figure 7a):

$$GS_{319} = 660 \dot{T}^{-0.22} (\mu\text{m}, R^2 = 0.81) \quad \text{Eqn. 2}$$

$$GS_{319R} = 311 \dot{T}^{-0.24} (\mu\text{m}, R^2 = 0.94). \quad \text{Eqn. 3}$$

In fact, the grains size of the refined microstructure is 1/2 of the non-refined microstructure.

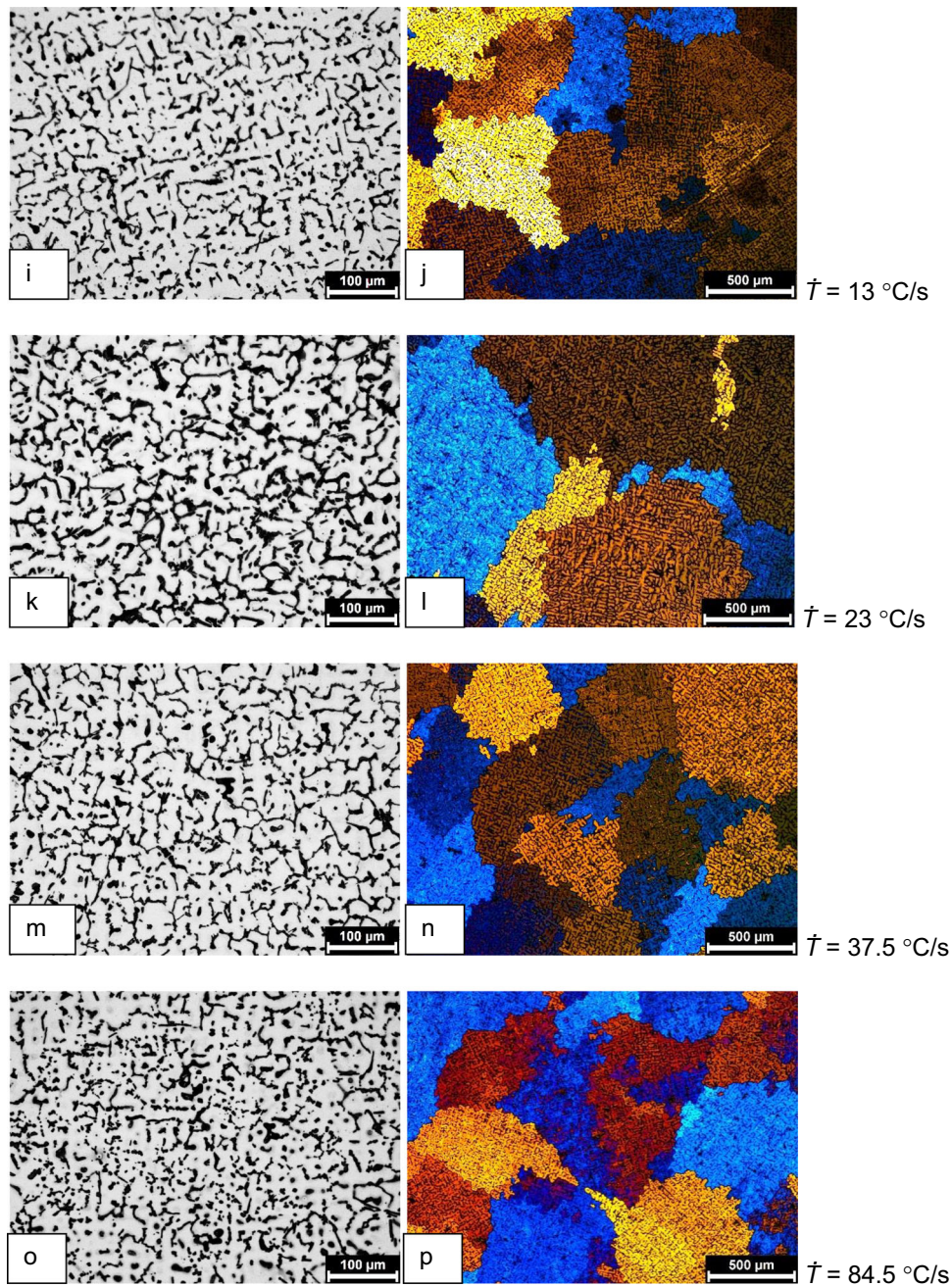


Figure 5. continued

The heterogeneity of the unrefined structure should be emphasized once again. However, for parameters λ_1 , λ_L and λ_2 , which are significantly affected by \dot{T} , the following equations can be generated:

$$\lambda_1 = 268 \dot{T}^{-0.36} \quad (\mu\text{m}, R^2 = 0.91) \quad \text{Eqn. 4}$$

$$\lambda_L = 62 \dot{T}^{-0.28} \quad (\mu\text{m}, R^2 = 0.91) \quad \text{Eqn. 5}$$

$$\lambda_2 = 36 \dot{T}^{-0.30} \quad (\mu\text{m}, R^2 = 0.95) \quad \text{Eqn. 6}$$

As they can predict the final microstructure of the part produced, these equations can be used to support the simulation of sand casting and die casting processes.

For a given value of \dot{T} , λ_1 is greater than λ_2 for both alloys, which agrees with the theory of dendrite growth during solidification.^{8,15–17} This difference is explained by the fact that primary dendrites grow with a large degree of freedom because of the ease with which the solute is distributed in the liquid at the growth interface. As primary dendrites form, secondary dendrites grow in the narrow primary interdendritic space in which the solute is trapped and segregated, resulting in slower growth kinetics for the secondary arms.²⁶ This effect is amplified for tertiary dendrites and so on.

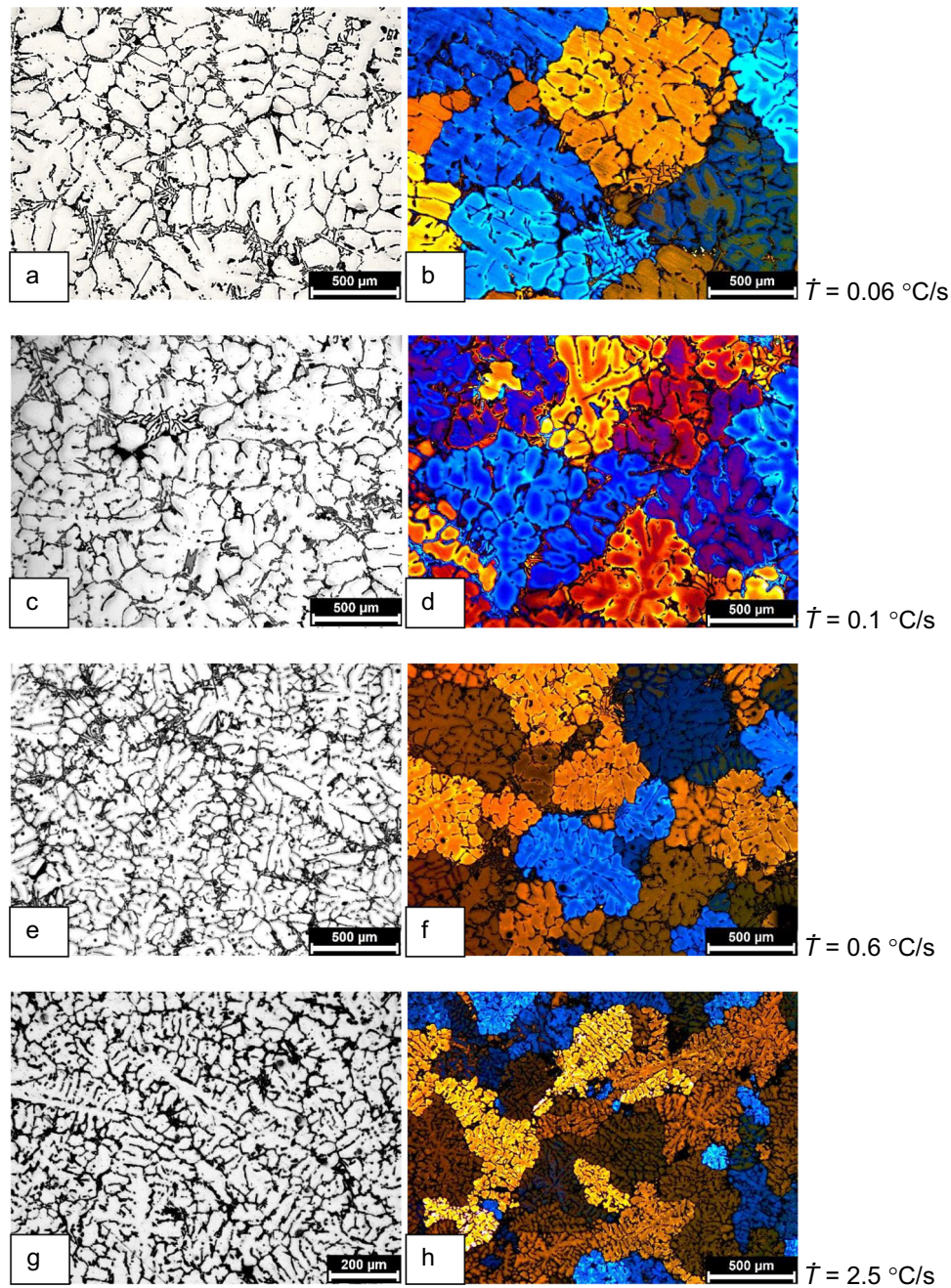


Figure 6. Microstructural evolution of 319R alloy with increasing cooling rate. Conventional B&W micrographs and color micrographs taken under polarized light for cooling rates of: (a) and (b) $\dot{T} = 0.06$ °C/s; (c) and (d) $\dot{T} = 0.1$ °C/s; (e) and (f) $\dot{T} = 0.6$ °C/s; (g) and (h) $\dot{T} = 2.5$ °C/s; (i) and (j) $\dot{T} = 6.5$ °C/s; (k) and (l) $\dot{T} = 13$ °C/s; (m) and (n) $\dot{T} = 23$ °C/s; and (o) and (p) $\dot{T} = 84.5$ °C/s.

The experimental growth laws are represented by the power function $a\dot{T}^{-b}$ with the coefficients $a(\lambda_1) = 268$ and $a(\lambda_2) = 36$. The microstructural parameters λ_1 and λ_2 follow different, progressively slower growth kinetics as \dot{T} increases. This is expressed by the exponent b , where $b(\lambda_1) = -0.36$ and $b(\lambda_2) = -0.30$. The values of the coefficient a and exponent b found here for the alloys studied are compatible with those reported in the literature for similar systems, e.g., $a(\lambda_1) = 250$ and $b(\lambda_1) = -0.55$ for Al-

5%Cu, Al-8 wt%Cu and Al-15 wt%Cu alloys¹⁵; $a(\lambda_1) = 220$ and $b(\lambda_1) = -0.55$ for Al-3 wt%Si, Al-5 wt%Si, Al-7 wt%Si and Al-9 wt%Si alloys¹⁵; and $a(\lambda_1) = 153$ and $b(\lambda_1) = -0.55$ for Al-6% Cu-1 wt%Si and Al-6 wt%Cu-4 wt%Si alloys.¹⁷ Note that all the microstructural parameter refers to a non-refined structures.^{15,16}

The data presented here indicate that the growth kinetics of λ_1 ($b = -0.36$) were not significantly affected by the

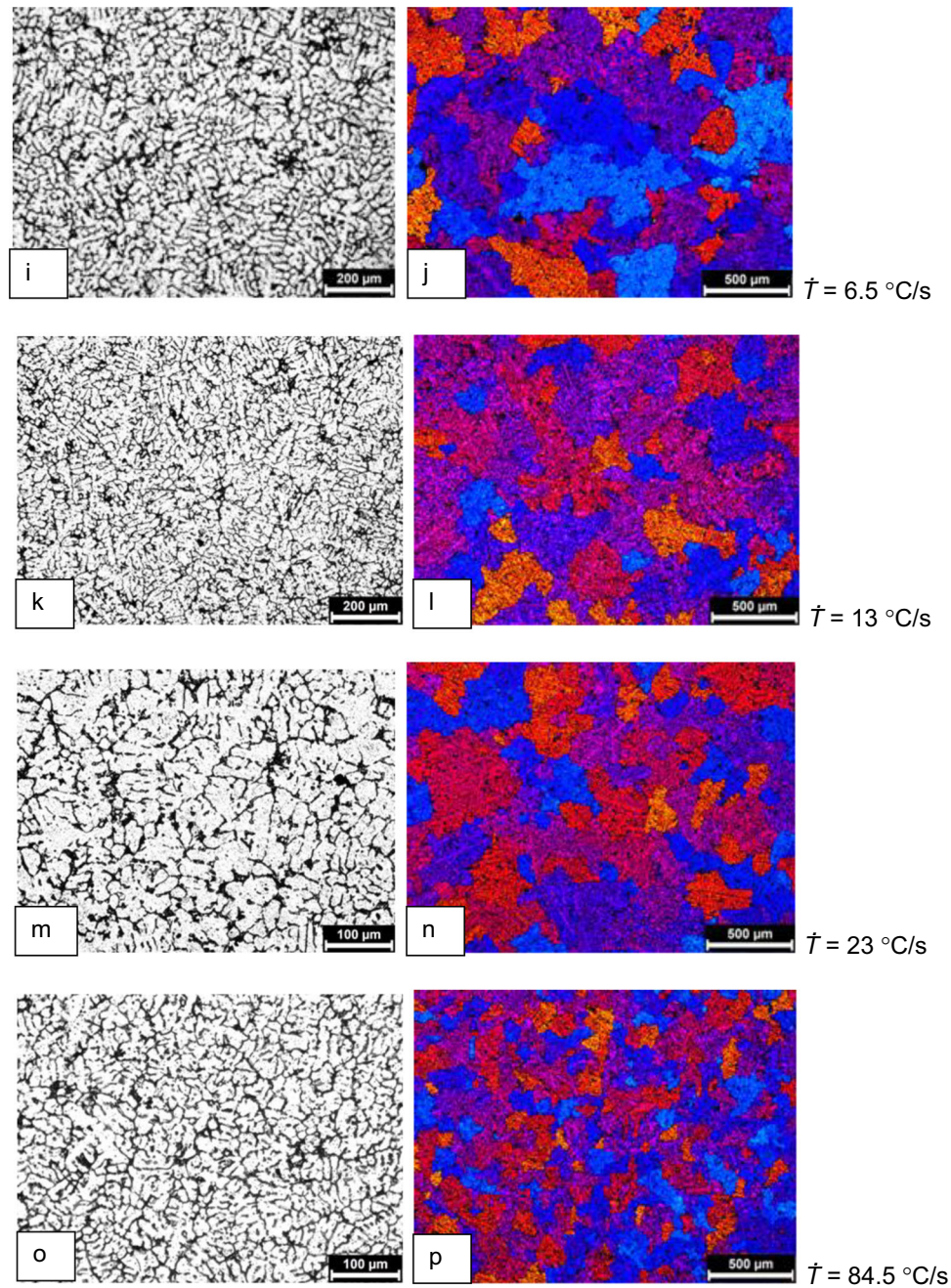


Figure 6. continued

addition of refiner. Similarly, in the case of the 319R alloy, the value of the exponent λ_2 is identical to that for the 319 alloy ($b = -0.30$).

As observed in³² for multicomponent Al alloys, the addition of chemical refiner does not affect the magnitude of secondary dendrite arms. The kinetic growth of λ_2 is exactly the same for both conditions studied here ($a = 36$, $b = -0.30$) and is in agreement with the values found in the literature, i.e., $a = 20.43$, $b = -0.33$ for Al-6 wt%Cu-1 wt%Si;¹⁴ $a = 14.59$, $b = -0.33$ for Al-6 wt%Cu-4 wt%Si alloys¹⁴; $a = 41$, $b = -0.33$ for Al-5.5 wt%Si-3 wt%Cu

alloys; and $a = 28$, $b = -0.33$ for Al-9 wt%Si-3 wt%Cu alloys.¹⁶

Figure 7c shows the correlation between λ_L and \dot{T} for 319 and 319R alloys. Again, the similarity between the individual models allowed the data to be fitted jointly, as shown in the graph, indicating that grain refining did not affect the change in λ_L with \dot{T} .

Figure 8 shows primary, average and secondary dendrite arm spacing against GS (Figure 8a λ_1 , Figure 8b λ_L and Figure 8c λ_2). Note that the dispersion of the data for 319

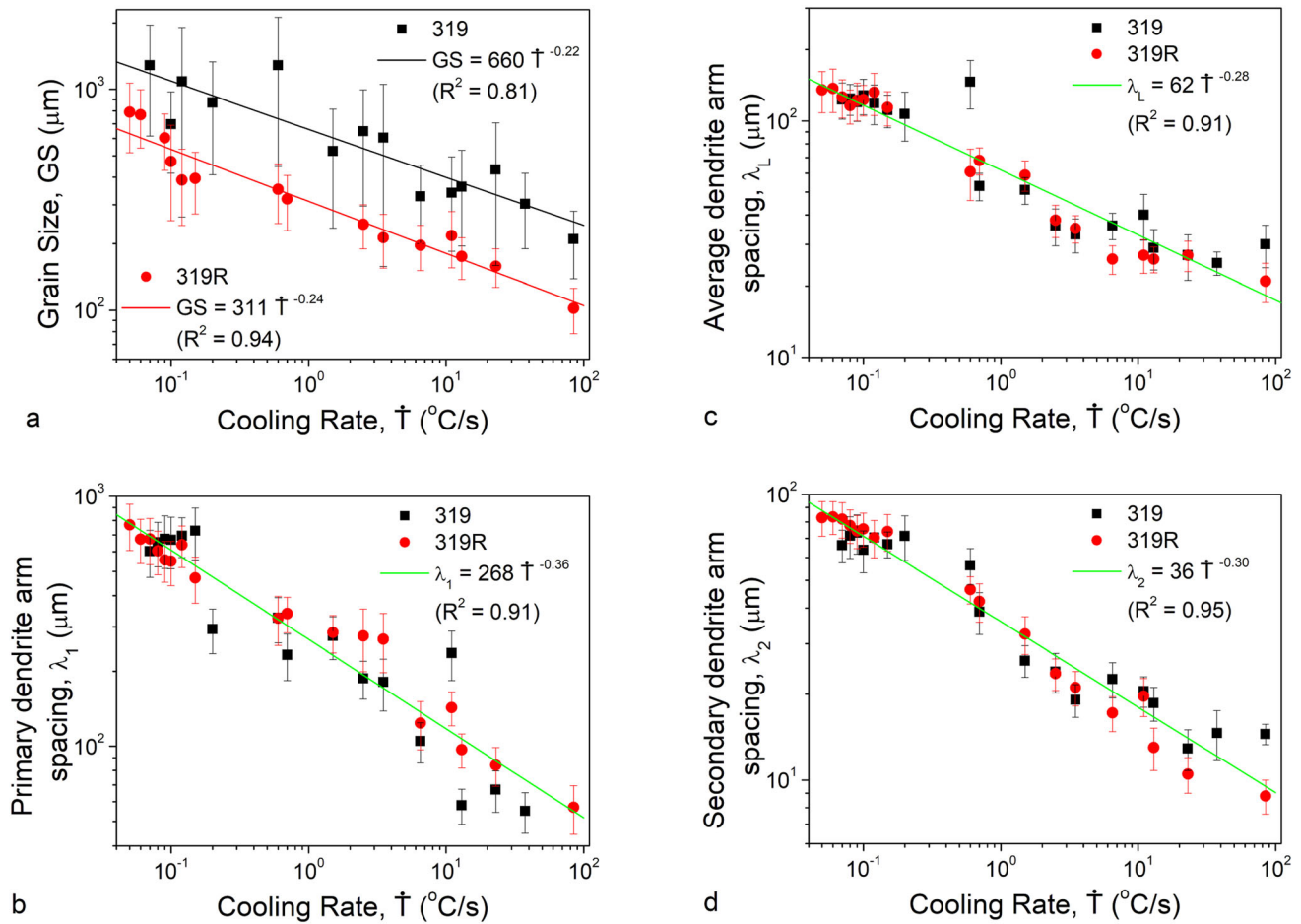


Figure 7. Values, trend lines and experimental equations for GS (a), λ_1 (b), λ_L (c) and λ_2 (d) in relation to the cooling rate \dot{T} for the 319 and 319R alloys.

alloy indicates the absence of a correlation. For 319R alloy, however, there is an excellent correlation, indicating that the larger GS, the larger λ_1 , λ_L and λ_2 (as expected). This alloy, to which grain refiner was added, has a more homogeneous microstructure, and all possible direct relationships resulted in a value of R^2 greater than 0.8. Note that for conventional dendritic structures, the grain size differs greatly from the primary dendritic spacing, but for refined structures, the relationship is direct, in fact $\lambda_1 = 0.9997 \text{ GS}$, or simple $\lambda_1 = \text{GS}$, with $R^2 = 0.8527$. It is clear that for unrefined structures, there is no limitation against the growth of the Al_x and the structure tends to present a three-dimensional skeleton forming a very complex structure, but for refined structures, due to the high number of nuclei formed, growth is limited, generating a situation in which a dendritic cell actually corresponds to a grain. In fact, this was observed by Kurz³⁴: “the primary spacing in an equiaxed structure is not well-defined and usually corresponds to the mean grain diameter.”

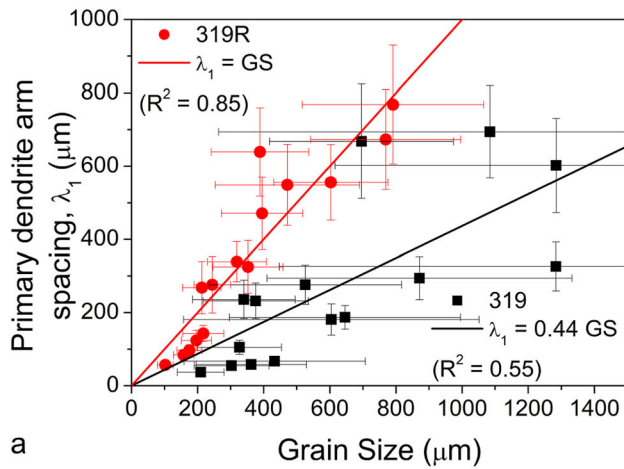
Figure 9 shows the correlation between λ_L and λ_1 and between λ_L and λ_2 . As expected, the more homogeneous the structure, the greater the correlation between the thermal parameters. λ_L , which is much simpler to measure, is

thus a good parameter for evaluating the microstructure. In the case of 319 alloy, λ_1 and λ_2 can be estimated with the following equations:

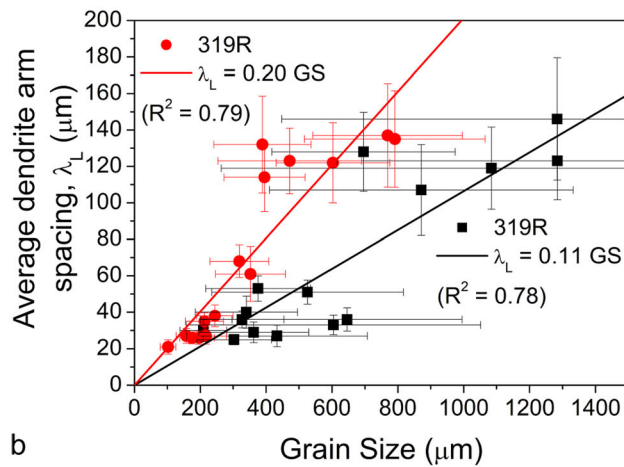
$$\lambda_1 = 4.92 \lambda_L - 11.92 \quad (\mu\text{m}, R^2 = 0.83) \quad \text{Eqn. 7}$$

$$\lambda_2 = 0.57 \lambda_L + 1.19 \quad (\mu\text{m}, R^2 = 0.93) \quad \text{Eqn. 8}$$

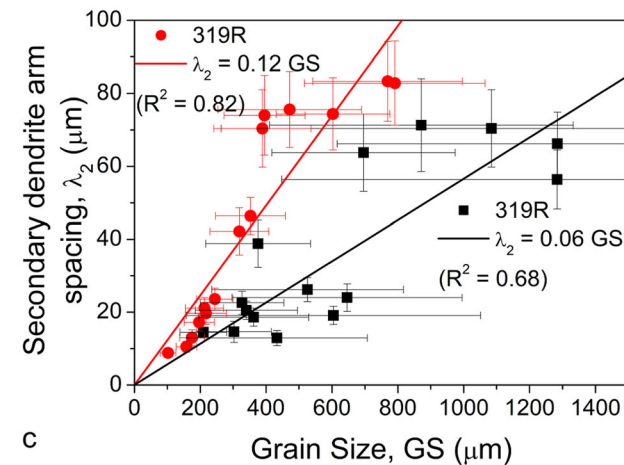
It should be noted that the values of λ_1 for the 319 alloy are lower than for the 319R alloy for $\dot{T} > 0.5$ $^{\circ}\text{C/s}$. At first sight, this may seem to be inconsistent with the fundamental role of grain refinement and the observed microstructure for these alloys. A possible explanation for this is the presence of dendrite fragments between neighboring Maltese crosses in the 319R alloy, as shown in Figure 10a. These dendrite fragments result in a higher average λ_1 measured by the triangle method because of the triangle's larger sides. This is shown by the dashed line in Figure 9a. There is a massive presence of dendrite fragments in the 319R alloy because of the radial growth caused by extensive nucleation. It should therefore be kept in mind that measurement of λ_1 by the triangle method for chemically refined alloys may not always be very accurate. To overcome this drawback, colored images can be used to enable the identification of fragments (as in Figure 10a) so



a



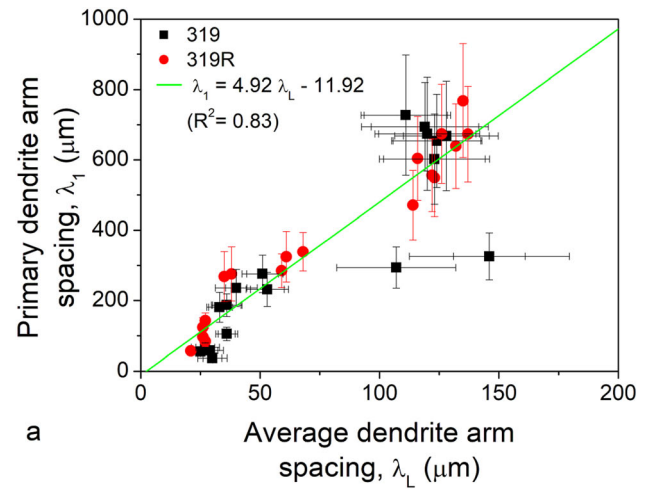
b



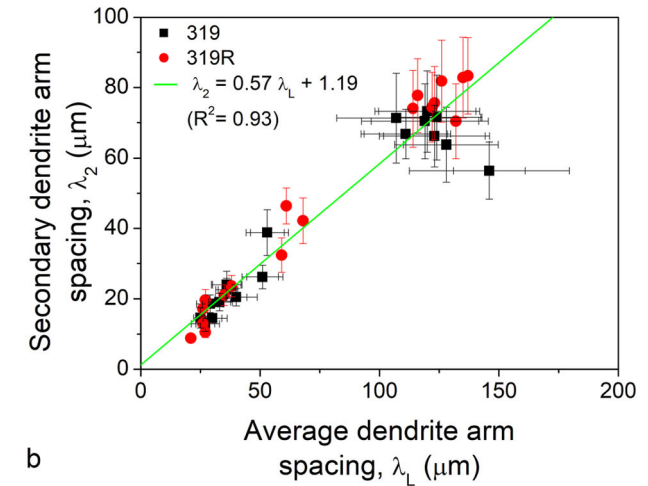
c

Figure 8. Relationship between grain size and dendrite arm spacing: (a) λ_1 , (b) λ_L and (c) λ_2 .

that these regions are avoided during the quantitative analysis. The morphological changes from Maltese-cross to rosette-like dendritic ramifications caused by the addition of chemical refiner are shown in Figure 10b and c, respectively.



a



b

Figure 9. Relationship between primary and secondary arm spacing and average dendrite arm spacing: (a) λ_1 and (b) λ_L and λ_2 .

Conclusions

Addition of Al-5Ti-1B [wt%] to 319 alloy as grain refiner had a significant effect on the observed GS. The resulting power law to describe the effect of cooling rate on grain formation had a proportionality constant $a(319) = 660$ ($\mu\text{ms}^\circ\text{C}^{-1}$) for the unrefined structure and $a(319R) = 311$ ($\mu\text{ms}^\circ\text{C}^{-1}$) for the refined alloy. However, the growth kinetics, represented by the exponent b , were similar: $b(319) = -0.22$ and $b(319R) = -0.24$. The grain refiner therefore only affects nucleation and not grain growth. In addition, the grain refiner did not significantly affect growth of the dendritic structure in terms of the primary and secondary dendrite spacing. The proportionality constant was $a(\lambda_1) = 268$ ($\mu\text{ms}^\circ\text{C}^{-1}$) and $a(\lambda_2) = 36$, while the growth exponent was $b(\lambda_1) = -0.36$ and $b(\lambda_2) = -0.30$. Thus, only the cooling rate significantly affects the formation of the primary and secondary morphology, i.e., λ_1 and λ_2 . A simpler analysis parameter, average dendrite arm spacing, λ_L , was introduced. This parameter, which is calculated using the Heyn intercept method, proved to have an excellent correlation with λ_1 and λ_2 and can be used to

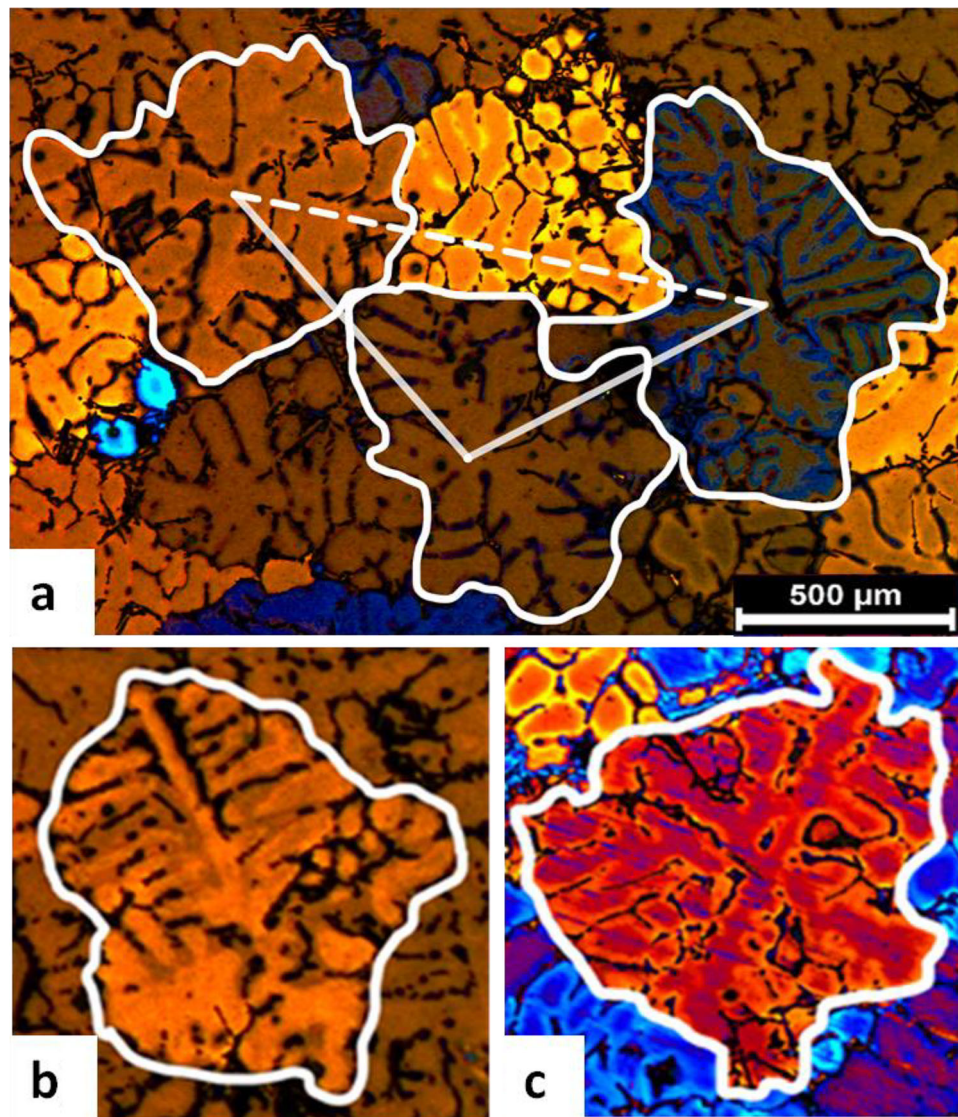


Figure 10. (a) Dendrite fragments between three neighboring dendrites; (b) Maltese-cross dendrite in 319 alloy;²⁵ rosette-like dendrite in 319R alloy.

estimate the final microstructure. The proportionality constant and growth exponent were $a(\lambda_L) = 62 \text{ (}\mu\text{m} \text{ } ^\circ\text{C}^{-1}\text{)}$ and $b(\lambda_L) = -0.28$.

Acknowledgements

The authors would like to thank the Brazilian research funding agencies FAPESP (São Paulo Research Foundation—projects 2009/08478-1, 2013/09961-3, 2015/22143-3, 2021/11439-0 and 2022/05050-5), CNPq (National Council for Scientific and Technological Development—projects 470572/2011-6 and 140918/2018-3) and CAPES (Federal Agency for the Support and Improvement of Higher Education—notice 23/2016, ref. no. 88881.131045/2016-01) for providing financial support for this study. The authors are also indebted to the Faculty of Mechanical Engineering at the University of Campinas for the practical

support very kindly provided.

Conflict of Interest On behalf of all authors, the corresponding author states that there is no conflict of interest.

Open Access This article is licensed under a Creative Commons Attribution 4.0 International License, which permits use, sharing, adaptation, distribution and reproduction in any medium or format, as long as you give appropriate credit to the original author(s) and the source, provide a link to the Creative Commons licence, and indicate if changes were made. The images or other third party material in this article are included in the article's Creative Commons licence, unless indicated otherwise in a credit line to the material. If material is not included in the article's Creative Commons licence and your intended use is not permitted by statutory regulation or exceeds the permitted use, you will need to obtain permission directly from the copyright holder. To view a copy of this licence, visit <http://creativecommons.org/licenses/by/4.0/>.

REFERENCES

1. J.R. Davies, *ASM specialty handbook—aluminum and aluminum alloys* (Novelty, Enschede, 1993)
2. B. Donadoni, G.L. de Gouveia, A. Garcia, J.E. Spinelli, J. Manuf. Process **54**, 14–18 (2000). <https://doi.org/10.1016/j.jmapro.2020.02.047>
3. B. Wang, J. Wang, X. Liu, Q. Li, X. Liu, Mater. Sci. Eng. A **858**, 144090 (2022). <https://doi.org/10.1016/j.msea.2022.144090>
4. A.M. Samuel, H.W. Doty, S. Valtierra, F.H. Samuel, Beta Al5FeSi phase platelets-porosity formation relationship in A319.2 type alloys. Int. J. Metalcasting **12**(1), 55–70 (2018). <https://doi.org/10.1007/s40962-017-0136-9>
5. M.C. Flemings, Metall. Trans. B **22**(3), 269–293 (1991). <https://doi.org/10.1007/BF02651227>
6. Z. Fan, Inter. Mater. Rev. **47**(2), 49–86 (2002). <https://doi.org/10.1179/095066001225001076>
7. M.S. Salleh, M.Z. Omar, J. Syarif, M.N. Mohammed, Inter. Sch. Res. Not. (2013). <https://doi.org/10.1155/2013/679820>
8. J.D. Hunt, S.Z. Lu, Metall. Trans. A **27**(3), 611–623 (1996). <https://doi.org/10.1007/BF02648950>
9. G.K. Sigworth, T.A. Kuhn, Int. J. Metalcasting **1**(1), 31–40 (2007). <https://doi.org/10.1007/BF03355416>
10. E. Vandersluis, N. Prabakaran, C. Ravindran, Inter. Metalcasting **14**, 37–46 (2020). <https://doi.org/10.1007/s40962-019-00329-w>
11. E. Aghaie, J. Stroh, D. Sediako, A. Rashidi, A.S. Milani, Mater. Sci. Eng. A **793**, 139899 (2020). <https://doi.org/10.1016/j.msea.2020.139899>
12. G.K. Sigworth, Int. J. Metalcasting **2**(2), 19–40 (2008). <https://doi.org/10.1007/BF03355425>
13. D. Bouchard, J.S. Kirkaldy, Metall. Mater. Trans. B **28**, 651–663 (1997). <https://doi.org/10.1007/s11663-997-0039-x>
14. M. Rappaz, W.J. Boettinger, Acta Mater. **47**(11), 3205–3219 (1999). [https://doi.org/10.1016/S1359-6454\(99\)00188-3](https://doi.org/10.1016/S1359-6454(99)00188-3)
15. O.L. Rocha, C.A. Siqueira, A. Metall. Mater. Trans. A **34**, 995–1006 (2003). <https://doi.org/10.1007/s11661-003-0229-3>
16. M.D. Peres, C.A. Siqueira, A. Garcia, J. Alloys Comp. **381**(1–2), 168–181 (2004). <https://doi.org/10.1016/j.jallcom.2004.03.107>
17. D.J. Moutinho, L.G. Gomes, O.L. Rocha, I.L. Ferreira, A. Garcia, Mater. Sci. Forum **730–732**, 883–888 (2012). <https://doi.org/10.4028/www.scientific.net/msf.730-732.883>
18. M. Tiryakioğlu, Metall. Mater. Trans. A **50**, 3030–3032 (2019). <https://doi.org/10.1007/s11661-019-05257-2>
19. J.A. Spittle, S.G.R. Brown, Mater. Sci. Technol. **21**(9), 1071–1077 (2005). <https://doi.org/10.1179/174328405X51839>
20. E. Quested, A.L. Greer, Acta Mater. **52**(13), 3859–3868 (2004). <https://doi.org/10.1016/j.actamat.2004.04.035>
21. L. Bolzoni, N. Hari Babu, Metall. Mater. Trans. A **50**(2), 746–756 (2019). <https://doi.org/10.1007/s11661-018-5017-1>
22. G. Salloum-Abou-Jaoude, P. Jarry, P. Celle, E. Sarrazin, Miner. Metals Mater. Ser. (2020). https://doi.org/10.1007/978-3-030-36408-3_134
23. A.M. Samuel, F.H. Samuel, H.W. Doty, S. Valtierra, Int. J. of Metalcasting **11**(2), 305–320 (2017). <https://doi.org/10.1007/s40962-016-0075-x>
24. A.M. Samuel, F.H. Samuel, H.W. Doty, S. Valtierra, Int. J. Metalcasting **11**(3), 475–493 (2017). <https://doi.org/10.1007/s40962-016-0089-4>
25. American Society for Testing and Materials, B179–18: standard specification for aluminum alloys in ingot and molten forms for castings from all casting processes (ASTM International, West Conshohocken, 2018). <https://doi.org/10.1520/B0179-18>
26. T. Soares, C. Cruz, A. Barros, A. Garcia, N. Cheung, Adv. Eng. Mater. **22**(6), 1901592 (2020). <https://doi.org/10.1002/adem.201901592>
27. R. Kakitani, R. Oliveira, R.V. Reyes, A.V. Rodrigues, F. Bertelli, A. Garcia, J.E. Spinelli, N. Cheung, Case Stud. Therm. Eng. **26**, 101144 (2021). <https://doi.org/10.1016/j.csite.2021.101144>
28. R. Oliveira, T.A. Costa, M. Dias, C. Konno, N. Cheung, A. Garcia, Mater. Today Comm. **25**, 101490 (2020). <https://doi.org/10.1016/j.mtcomm.2020.101490>
29. M. Gündüz, E. Çadırılı, Mater. Sci. Eng. A **327**(2), 167–185 (2002). [https://doi.org/10.1016/S0921-5093\(01\)01649-5](https://doi.org/10.1016/S0921-5093(01)01649-5)
30. G.L. Brollo, C.T.W. Proni, E.J. Zoqui, Metals **8**(5), 332 (2018). <https://doi.org/10.3390/met8050332>
31. D. Kim, J. Kim, S. Wenner, E. Thronsen, C.D. Marioara, R. Holmestad, E. Kobayashi, Mater. Charact. **173**, 110863 (2021). <https://doi.org/10.1016/j.matchar.2020.110863>
32. M. Rappaz, P. Thévoz, Acta Metall. **35**(7), 1487–1497 (1987). [https://doi.org/10.1016/0001-6160\(87\)90292-6](https://doi.org/10.1016/0001-6160(87)90292-6)
33. M. Easton, D. St John, Metall. Mater. Trans. A **41**(6), 1528–1538 (2010). <https://doi.org/10.1007/s11661-010-0183-9>
34. W. Kurz, D.J. Fisher, *Fundamentals of solidification*, 4th edn. (Trans Tech Publications, Wollerau, 1998), p.305. (ISBN: 0878498044)

Publisher's Note Springer Nature remains neutral with regard to jurisdictional claims in published maps and institutional affiliations.